Radiative decoupling and coupling of nuclear oscillators by stepwise Doppler-energy shifts

P. Schindelmann, U. van Bürck, and W. Potzel*

Physik-Department E15, Technische Universität München, D-85748 Garching, Germany

G. V. Smirnov and S. L. Popov

Russian Research Center "Kurchatov Institute," 123182 Moscow, Russia

E. Gerdau, Yu. V. Shvyd'ko, J. Jäschke, and H. D. Rüter

Institut für Experimentalphysik, Universität Hamburg, D-22761 Hamburg, Germany

A. I. Chumakov and R. Rüffer

European Synchrotron Radiation Facility (ESRF), P.O. Box 220, F-38043 Grenoble, France

The nuclear forward scattering of synchrotron radiation (NFSSR) of two spatially separated but otherwise identical stainless-steel targets is strongly influenced by the application of approximately stepwise Doppler energy shifts to one of the targets in synchronization with the synchrotron radiation (SR) pulse. The decisive role of radiative coupling in NFSSR, i.e., the influence of the radiation field emitted by the upstream target on the oscillators of the downstream target, has been clarified in decoupling and coupling experiments. In decoupling experiments, radiative coupling is initially strong and becomes drastically reduced when the Doppler motion is started some time interval after the prompt excitation of the two-target system by the SR pulse. In addition, due to the Doppler energy shift a pronounced quantum beat (QB) develops. Depending on the starting time of the Doppler motion, the onset of the QB manifests itself as a rapid decrease or increase of the NFSSR intensity. In coupling experiments, the Doppler motion is started before the SR pulse arrives and a QB is observed right after the SR excitation. Some time interval thereafter the motion is stopped, so that the resonance energies of both targets coincide. As a consequence, the QB disappears and radiative coupling can develop. Depending on the time when the Doppler motion is stopped, this coupling can be responsible for the main contribution to the NFSSR intensity. The changes of the evolution due to decoupling or coupling also strongly depend on the details of the Doppler velocity profile. We show that precise velocity profiles on a nanosecond time scale can be derived by applying the method of quantum-beat analysis and independently by a fitting procedure based on the dynamical theory of scattering. All NFSSR evolutions investigated are interpreted and quantitatively described within the dynamical theory in terms of the interference of the wave fields reemitted by the scattering system.

I. INTRODUCTION

In several recent papers [1–5] it has been emphasized that radiative coupling of nuclear oscillators plays an important role in nuclear resonant scattering in general and in nuclear forward scattering of synchrotron radiation (NFSSR) in particular [6]. Radiative coupling intrinsically determines the formation and decay of nuclear excitons in targets [7,8]. It is the interaction of the secondary radiation in multiple scattering within an ensemble of nuclear oscillators: after the excitation of the nuclear oscillators by the synchrotron radiation (SR) pulse, the coherent radiation field reemitted from upstream nuclei in such an ensemble can resonantly interact with nuclei further downstream. This interaction leads to several highly characteristic features of NFSSR. For example, the coherent enhancement or speeding up of the initial decay and the formation of dynamical beats are consequences of the coupling of the nuclear oscillators in the ensemble via the propagating coherent radiation field [1,3,7–14]]. Due to the initial in-phase excitation of the nuclei by

the SR pulse and because of spatial coherence in forward scattering, this radiation field propagates in the downstream direction. Thus radiative coupling in NFSSR is a unidirectional process. Upstream nuclei can influence downstream nuclei, but not vice versa.

In the usual NFSSR experiment it is difficult to single out the properties of radiative coupling because it affects downstream nuclei within the same target. In the present paper we use a setup of two spatially separated but otherwise identical targets A and B mounted downstream behind each other. In such a system radiative coupling between the targets can be distinguished from that within each target. The former occurs because the nuclei in the downstream target B can resonantly interact with the delayed coherent radiation reemitted in the forward direction from the upstream target A. As a consequence, the field that target B emits is a superposition of two parts, its own radiation field $\mathcal{B}$, which is reemitted after excitation by the SR pulse and which in our case of identical targets has the same amplitude and time dependence as the field $\mathcal{A}$ emitted by the upstream target A, and the radiation field $\mathcal{R}$ that originates from the excitation of the nuclei in target B due to the driving action of the field $\mathcal{A}$ reemitted from the target A. To emphasize its origin we call this field $\mathcal{R}$ the radiative coupling field.
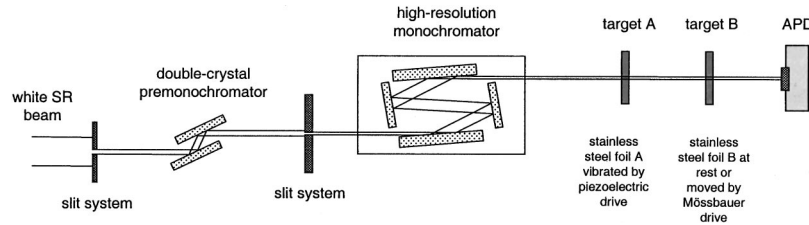
*Email address: wpotzel@ph.tum.de

FIG. 1. Scheme of the experimental setup for investigating the time response of the ^{57}Fe nuclei in two separated SS targets *A* and *B* to excitation by a synchrotron radiation pulse. Target *A* is vibrated on a nanosecond time scale according to various velocity profiles by a piezoelectric drive. Target *B* can be moved at constant velocity by a double-loudspeaker drive. The NFSSR intensity is detected by an avalanche photodiode (APD).

The central issue of this paper is the investigation of the radiative coupling field. This can be achieved by comparing the field $\mathcal{B}$ of target *B* alone with the total field $\mathcal{B}+\mathcal{R}$ that *B* emits when target *A* is also present. To experimentally determine the field $\mathcal{B}+\mathcal{R}$ we use the following method. Keeping target *B* stationary, a Doppler energy shift is applied to the nuclei in the upstream target *A* by an approximately stepwise velocity profile in synchronization with the SR pulse. Thus the oscillator ensembles of both targets are energetically separated and radiative coupling is drastically reduced if the energy shift is much larger than the linewidth of the oscillators in the ensemble. The radiation fields reemitted from the two targets interfere. From the characteristics of the interference patterns both fields can be determined and, in addition, information on the radiative coupling field $\mathcal{R}$ can be obtained. In spite of the energy separation, the field $\mathcal{R}$ can be of importance after decoupling until late times because of the long lifetime of the excited nuclear state. We applied this method to two very different cases. (1) The Doppler motion causing the decoupling of both targets was started some time interval after the arrival of the SR pulse. Thus both targets were first coupled for this time interval before decoupling occurred. (2) The motion was already started before the SR pulse and then stopped after some time interval. Thus the targets were first decoupled for this time interval and thereafter coupling started.

In both cases detailed discussions of the results will be given within the dynamical theory of nuclear forward scattering. The interpretation of the results is based on a theoretical description of the total response of the two-target system in terms of interference phenomena between three different wave fields: the fields $\mathcal{A}$ and $\mathcal{B}$ reemitted by the two individual targets if each target were present alone and the coupling wave field $\mathcal{R}$.

The paper is organized as follows. Section II describes the experimental setup, the development of a special piezoelectric Doppler drive working on a nanosecond time scale, and the method of synchronization of the Doppler motion with the SR pulse. In Sec. III A, the velocity calibration of the piezoelectric drive is discussed. Section III B presents the results and detailed interpretations for the two types of experiment: decoupling (Sec. III B 1) and coupling (Sec. III B 2) of the two targets. A short summary and conclusions are given in Sec. IV.

II. EXPERIMENTAL DETAILS

A. Experimental setup

The experimental setup is depicted in Fig. 1. In the first step the large bandwidth of the SR beam is reduced to a few eV by a Si(111) double-crystal premonochromator. The SR pulse, which is typically 100 ps in length, is further monochromatized to a bandwidth of a few meV around 14.4 keV by a four-bounce high-resolution monochromator [15,16] and thereafter excites the nuclei of the targets *A* and *B*. Target *A* is mounted on a piezoelectric polyvinylidene (PVDF) foil and can be moved with a trapezoidal displacement profile on a nanosecond time scale by applying trapezoidal voltage changes to the PVDF foil. This motion of target *A* was synchronized to the excitation of the targets by the SR pulse via a phase-locked-loop circuit as described below. Target *B* is kept stationary or can be moved at constant velocity by a Mössbauer drive of the double-loudspeaker type. A fast-avalanche photodiode [17–19] was used to detect the radiation reemitted by both targets in the forward direction. The time dependence of this nuclear forward-scattering intensity was digitally stored.

Targets *A* and *B* were made from stainless-steel (SS) foils of composition $Fe_{55}Cr_{25}Ni_{20}$ enriched to 95% in ^{57}Fe. Both targets had the same thickness of ~ 1.2 μm corresponding to a Mössbauer thickness $T \approx 9.3$ [3]. They were kept at room temperature. The SR experiments were performed at HASY-LAB (Hamburg) at the wiggler beamline BW4 of the DORIS storage ring, and at the undulator beamline ID22N of the European Synchrotron Radiation Facility (ESRF) in Grenoble.

B. Piezoelectric Doppler drive

To perform the experiments, the Doppler drive had to fulfill three main requirements as closely as possible: the mo-
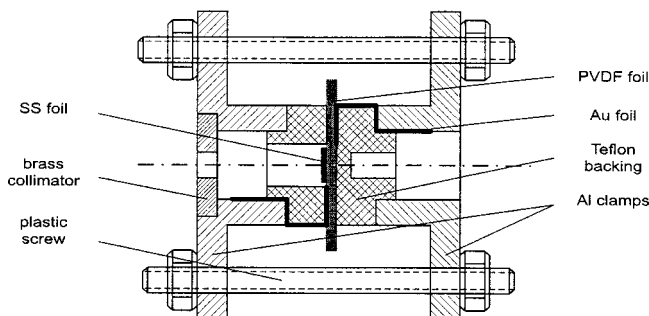

FIG. 2. Details of the piezoelectric drive. The PVDF foil which carries a SS target is glued to the Teflon backing. Electrical contacts to the PVDF foil are provided by thin Au stripes.
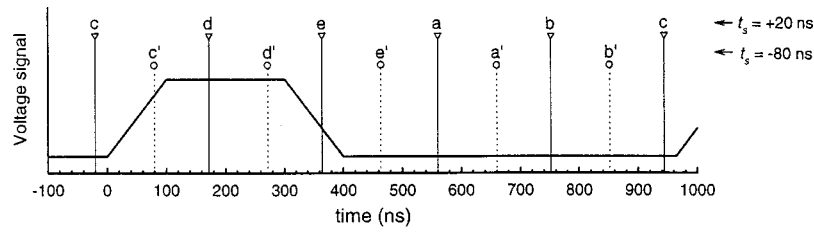
FIG. 3. Time positions of the five SR excitation pulses covering the trapezoidal voltage signal applied to the piezoelectric drive. Two sets $(a,b,\ldots,e)$ and $(a',b',\ldots,e')$ with different time shifts t_s are indicated. With $t_s = +20$ ns for the SR pulse c, the voltage signal starts 20 ns after the SR pulse; with $t_s = -80$ ns, the voltage signal is switched on 80 ns before the SR pulse c'.

tion of the PVDF foil together with the SS foil (target A) should be homogeneous, like the motion of a piston, over the cross section of the SR beam; the rising and falling edges of the trapezoidal motion should be on the nanosecond time scale yielding Doppler velocity shifts up to ~ 10 mm/s corresponding to ~ 100 natural linewidths Γ; the trapezoidal displacement should tightly follow the applied voltage signal. For example, after the rising and after the falling edges the velocity should be as close to zero as possible. We found that piezoelectric PVDF foils offer a good although by no means perfect solution.

The main features of our piezoelectric Doppler drive are shown in Fig. 2. It is based on earlier designs used in conventional Mössbauer measurements with radioactive sources as described in Refs. [20–23], however, it also features several important modifications to comply with special requirements of NFSSR experiments.

PVDF foils of 9 μm thickness with metallic NiCu or NiAl coating [24] were used as piezoelectric drivers. The enriched SS foils of ~ 1.2 μm thickness and 5 mm diameter were glued to the PVDF material [25]. Thereafter the metallic coating of the PVDF foils was removed by etching with 2.5M FeCl$_3$ solution, except for center disks of 6 mm diameter and a ~ 2-mm-wide contact stripe on each side of the PVDF foil. In this way the electric capacitance of the piezoelectric drive was reduced, allowing us to reach the required slopes of the rising and falling edges of the trapezoidal motion [25]. In addition, for pistonlike motion the use of a Teflon (polytetrafluoroethylene) backing proved to be essen-

tial [23]. The PVDF piezoelectric foil was tightly glued to the Teflon backing (see Fig. 2) which had been previously coated with a thin Ag layer. The PVDF foil on the Teflon backing and a Teflon front piece were rigidly aligned by two aluminum clamps, one of which also carried a brass collimator. Electrical contacts to the piezoelectric driver were ensured via two gold stripes of 3 mm width and 10 μm thickness each.

As indicated in Fig. 2, the centers of the Teflon parts were removed completely (left) or partially to a thickness of ~ 1.2 mm (right) to reduce electronic absorption of the 14.4 keV synchrotron radiation. This is a compromise, since the Teflon backing should be made rather thick [22,23] in order to absorb acoustic waves still present in the driving system after the rising and falling edges of the trapezoid where under ideal conditions the motion should have stopped abruptly. Further details are given in Ref. [25]. The performance of our piezoelectric drive will be discussed in Sec. III A below.

C. Synchronization of the trapezoidal motion with the SR pulse

The synchronization was achieved by using the bunch clock of the storage ring as a timing signal. It appears once for every turn of one of the electron bunches. This timing signal first passed an adjustable delay box where delays between -128 and $+128$ ns in steps of 0.5 ns could be selected and then drove the synchronization stage of the rf generator (Wavetek, model 81). Operated in the ''trigger mode,'' the
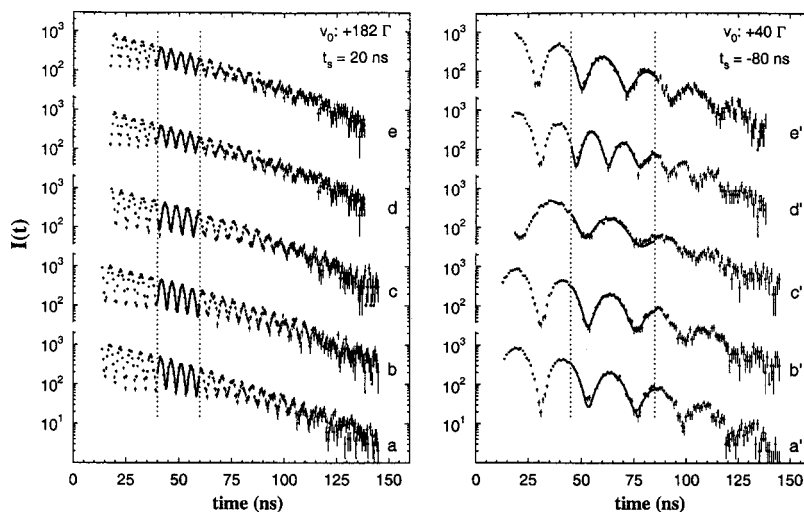

FIG. 4. Time dependences recorded in quantum-beat analysis experiments for $t_s = +20$ ns and constant Doppler velocity v_0 corresponding to $+182\Gamma$ (left) and $t_s = -80$ ns and v_0 corresponding to $+40\Gamma$ (right). The labels $a,b,\ldots,e$ and $a',b',\ldots,e'$ correspond to the SR excitations depicted in Fig. 3. The full lines through the data points are fits by the computer program MOTIF within the time intervals between 40 and 60 ns (left) and 45 and 85 ns (right) as indicated by the vertical broken lines.
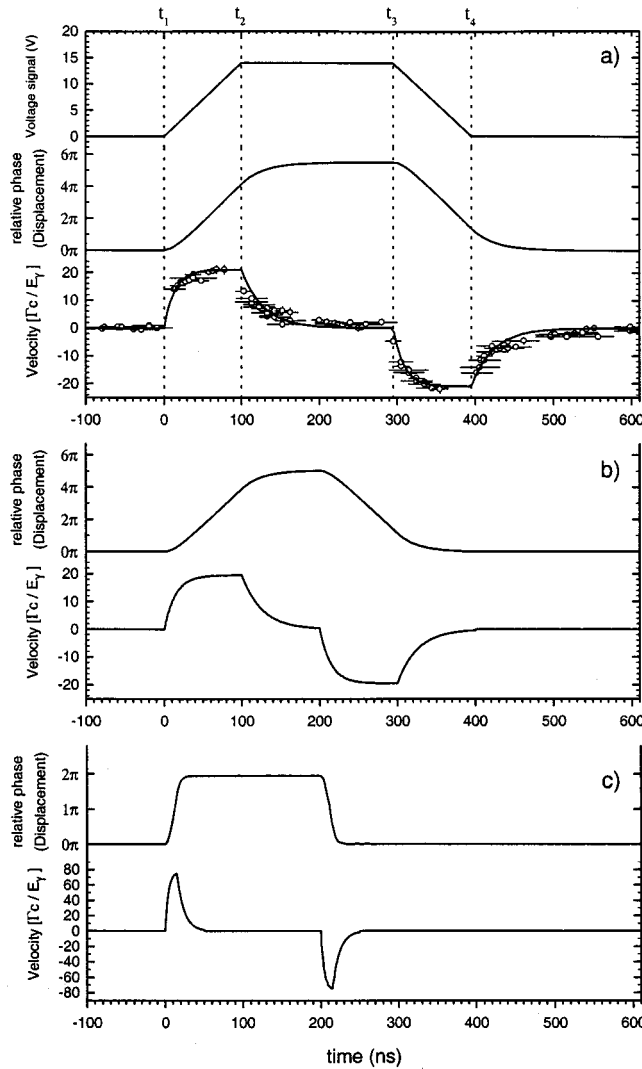
FIG. 5. The three velocity (displacement) profiles used in the experiments. Profile (a): ideal voltage signal applied to the piezoelectric drive (top); experimentally achieved displacement (middle) and velocity (bottom) profiles as determined by the quantum-beat analysis method. Profiles (b) and (c) were derived from computer simulations based on the dynamical theory of scattering as described in the text.

generator produced one trapezoidal voltage signal for every pulse of the bunch clock. This trapezoidal signal was amplified by a broadband amplifier (Amplifier Research, model 75A220) to amplitudes of typically 14 V and fed to the piezoelectric driver (see Fig. 2). No feedback control was applied.

Three different trapezoidal motion profiles were selected for our experiments: (a) rising (Δt_r) and falling (Δt_f) edges of the trapezoid of $\Delta t_r = \Delta t_f \approx 100$ ns and a dwell time (Δt_u) in the upper voltage level of $\Delta t_u \approx 200$ ns, (b) a profile with $\Delta t_r = \Delta t_f \approx 100$ ns and $\Delta t_u \approx 100$ ns, and (c) a profile with $\Delta t_u \approx 150$ ns and very rapid rise and fall times (see Sec. III A below). In all three cases considerable deviations from linearly rising and falling edges were observed as might be expected from the capacitorlike properties of the piezoelectric driver. The exact profiles are described below. In the data

analysis, the actual trapezoidal motion profiles were taken into account by the fitting procedure (see Sec. III). During the measurements the signal applied to the PVDF foil was monitored all the time on an oscilloscope to guarantee stable operating conditions of the piezoelectric driver.

The delay box allowed a variation of the start of the trapezoidal signal with respect to the prompt detector pulses originating from the $\sim$100-ps-long SR flash. These prompt detector pulses marked time $t = 0$ in the time dependences of the NFSSR intensity. In addition, depending on the filling mode of the storage rings, up to five time dependences with observation windows of typically 200 ns each were recorded in parallel with a repetition rate of the bunch clock of typically 1 MHz.

III. RESULTS AND DISCUSSION

A. Analysis of the motion of the piezoelectric drive: Quantum-beat analysis

For the development and optimization of the piezoelectric drive, Mössbauer spectroscopy in the energy as well as in the time domain [22,23] using radioactive ^{57}Co sources was applied. For example, in this way the drive was optimized for pistonlike motion and as low as possible contributions of unwanted vibrations, e.g., those due to acoustic waves inside the PVDF foil. Using this technique also the optimal thickness for the Teflon backing was found. Further details of drive development using Mössbauer techniques are given in Ref. [25]. Still, it turned out that an analysis and calibration of the motion of the piezoelectric drive under operational conditions at the synchrotron beamline was important.

Our analysis of the motion of the piezoelectric drive is based on the following concept. One target (A in Fig. 1) consisted of the SS foil on the piezoelectric drive; the second target B (of the same SS material) was mounted on a Mössbauer drive of the double-loudspeaker type and moved with constant velocity v_0. If target A is at rest (zero voltage applied to the PVDF foil), the Mössbauer resonance energy E_γ of the nuclei in target B is Doppler shifted by $(v_0/c)E_\gamma$ with respect to target A. The two wave fields reemitted by the targets after the excitation by the SR pulse interfere, which results in a quantum-beat (QB) pattern [6,26,10]. The period of the QB is determined by the velocity v_0. If, in addition, the piezoelectric drive is switched on in synchronization with the SR pulse, the relative velocity between the targets A and B is determined by the sum of v_0 and the instantaneous velocity $v(t)$ of A due to its trapezoidal motion. Thus the original QB period is modulated by the additional velocity dependence of target A. Therefore an analysis of the QB pattern allows the determination of this velocity dependence. This method has been called quantum-beat analysis (QBA). It has previously been used to investigate motions of or within a scattering system relative to a reference target [25,27–30].

The QBA was performed for the trapezoidal motion profile (a) with $\Delta t_r = \Delta t_f \approx 100$ ns and $\Delta t_u \approx 200$ ns (see Sec. II C above) at the wiggler beamline BW4 at HASYLAB in Hamburg. The storage ring was operated in the five-bunch mode. Thus during one trapezoid cycle of 964 ns period (the same period as the synchrotron bunch clock) five SR pulses
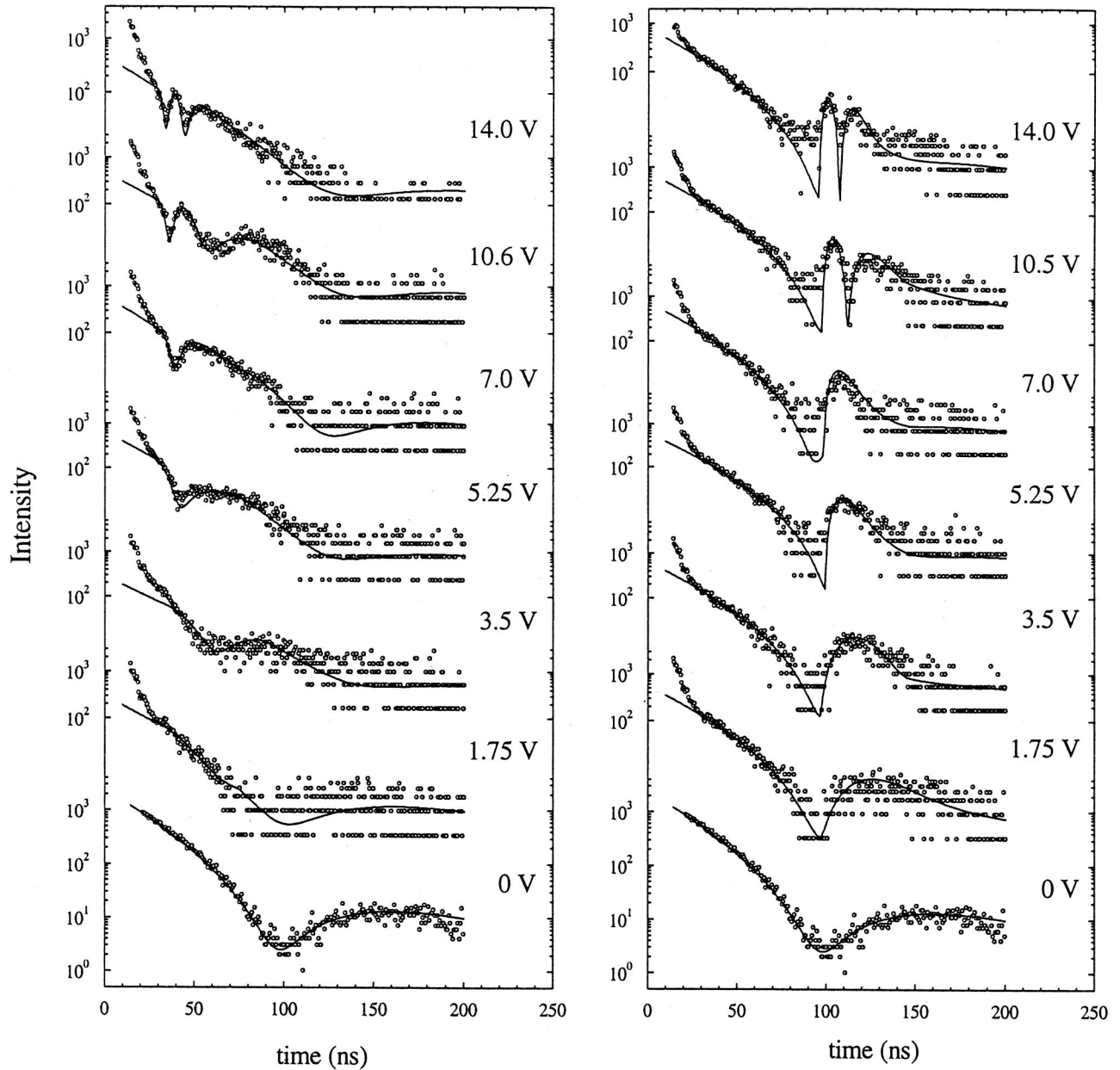
FIG. 6. NFSSR of two separated SS targets of ~1.2 μm thickness (Mössbauer thickness $T \approx 9.3$) each, recorded at various amplitudes of the voltage signal applied to the piezoelectric drive (target A). The motion profile (c) of Fig. 5(c) was used. Two different decoupling times t_d were selected. The SR pulse occurred at $t = 0$. The onset of decoupling at $t_d \approx 25$ ns (left) is noticed as a rapid drop of the NFSSR intensity and the development of QB dips. For $t_d \approx 95$ ns (right) the quantum beats start with a rapid rise of the NFSSR intensity leading to QB spikes. The full lines through the data points are the results of theoretical calculations according to Eq. (3) based on the theory of nuclear forward scattering.

arrived, displayed as $a-e$ in Fig. 3, which gave rise to five time dependences covering approximately equidistant intervals of about 190 ns each. These five time dependences were recorded in parallel. With two appropriately shifted sets of measurements, the trapezoid is scanned by altogether ten different time dependences starting at times marked by $a-e$ and $a'-e'$ in Fig. 3. In the experiment, we selected two shifts $t_s = +20$ and -80 ns between the leading edge of the trapezoid and the SR pulses c and c', respectively (see Fig. 3). In addition, the QBA was performed twice using two different constant velocities v_0 corresponding to Doppler

shifts of 40Γ and 182Γ. As examples, Fig. 4 displays the five QBA time dependences for $(v_0/c)E_\gamma = 182\Gamma$ and $t_s = +20$ ns (left) and those for $(v_0/c)E_\gamma = 40\Gamma$ and $t_s = -80$ ns (right). Taking time intervals of one QB period or longer and using Fig. 3 as a guide for selecting such intervals, the motion profile for target A was derived. The solid lines through the data points in Fig. 4 represent fits within the time interval between the vertical dashed lines using the computer program MOTIF [31]. From these fits the instantaneous velocity $v(t)$ of target A at that particular time interval is obtained. With maximal Doppler shifts of ~21Γ and
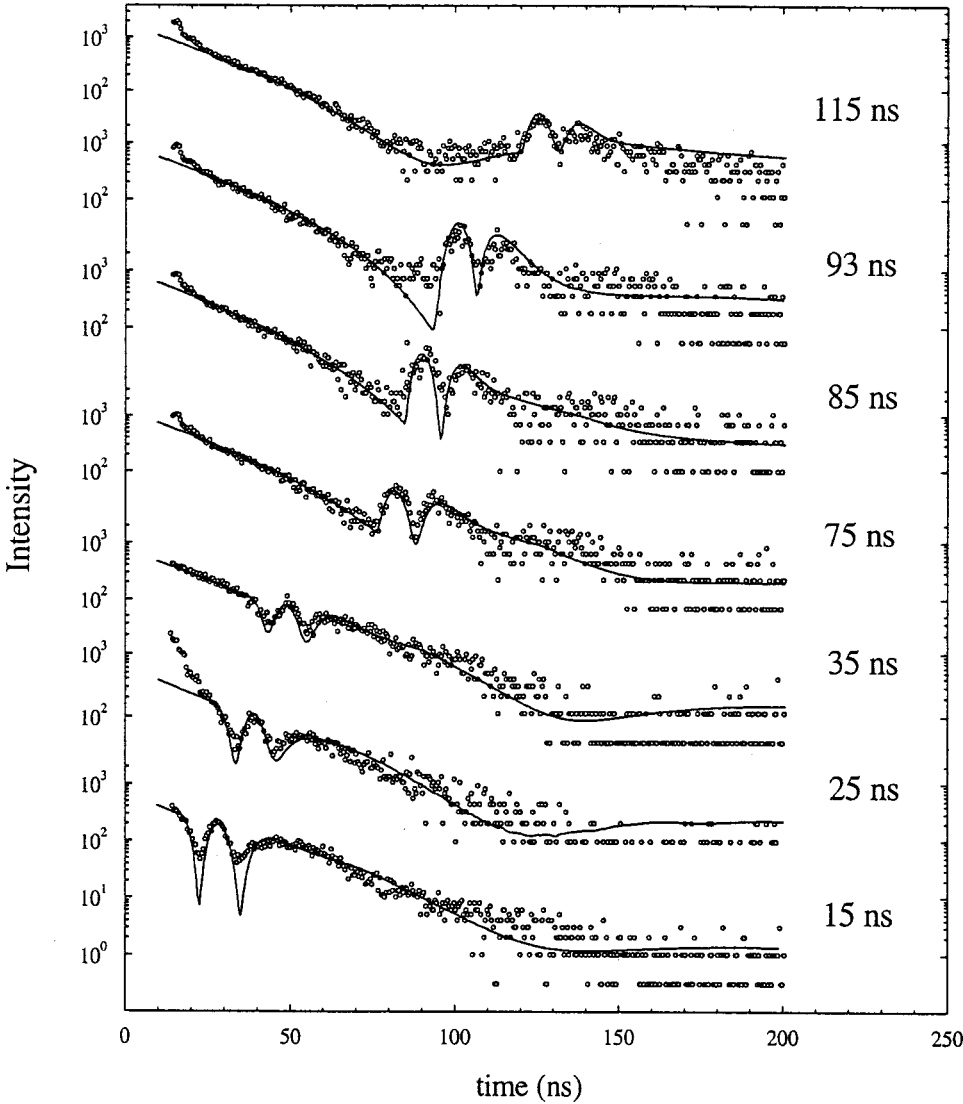
FIG. 7. NFSSR of two separated SS targets recorded with a voltage signal of 14 V at various decoupling times t_d. Note the transition from QB dips to QB spikes with increasing t_d. The contrast of the QB goes through a minimum at $t_d \approx 35$ ns. Other details as in Fig. 6.

$\sim 77\Gamma$ caused by the trapezoidal motions (the motion profiles are discussed below), a decrease (increase) of the original QB period is easily recognizable in curve d' (curve c) of Fig. 4. The original QB period is observed for the time dependences a, b and a',b' where the piezoelectric drive is found to be almost at rest. The much shorter QB period in the left-hand picture allows us to use shorter time intervals in the fitting procedure and thus a larger number of sampling points on the trapezoidal motion profile can be reached.

All QBA time dependences of Fig. 4 show a diminishing contrast of the QB patterns at late times. The main reason is the nonideal constant-velocity motion of the double-loudspeaker drive where a slight jitter of the velocity v_0 causes no harm at early times but a fading QB contrast at late times. A second reason for the fading contrast is that the motion of the piezoelectric drive is not fully pistonlike over the cross section of the SR beam.

The results of the QBA are summarized in Fig. 5(a). The top curve shows the form of the applied trapezoidal voltage signal which ideally would result in a stepwise velocity profile. The bottom curve of Fig. 5(a) exhibits the velocity profile actually achieved. The vertical error bars, which have

about the same size as the circles of the data points, represent the accuracy of the Doppler velocities as derived from the MOTIF fitting procedure. The horizontal error bars denote the length of the time interval used in the fits of the QBA time dependences to derive the instantaneous velocity for this particular time interval.

The experimental data of the velocity profile $v(t)$ are well represented by four exponential-type segments:

$$
\begin{aligned}
v(t) = &\ \Theta(t-t_1)v_{\max}\left(1-\exp\left\{-\frac{t-t_1}{\tau_1}\right\}\right) \\
&- \Theta(t-t_2)v_{\max}\left(1-\exp\left\{-\frac{t-t_2}{\tau_2}\right\}\right) \\
&- \Theta(t-t_3)v_{\max}\left(1-\exp\left\{-\frac{t-t_3}{\tau_3}\right\}\right) \\
&+ \Theta(t-t_4)v_{\max}\left(1-\exp\left\{-\frac{t-t_4}{\tau_4}\right\}\right),
\end{aligned}
\tag{1}
$$

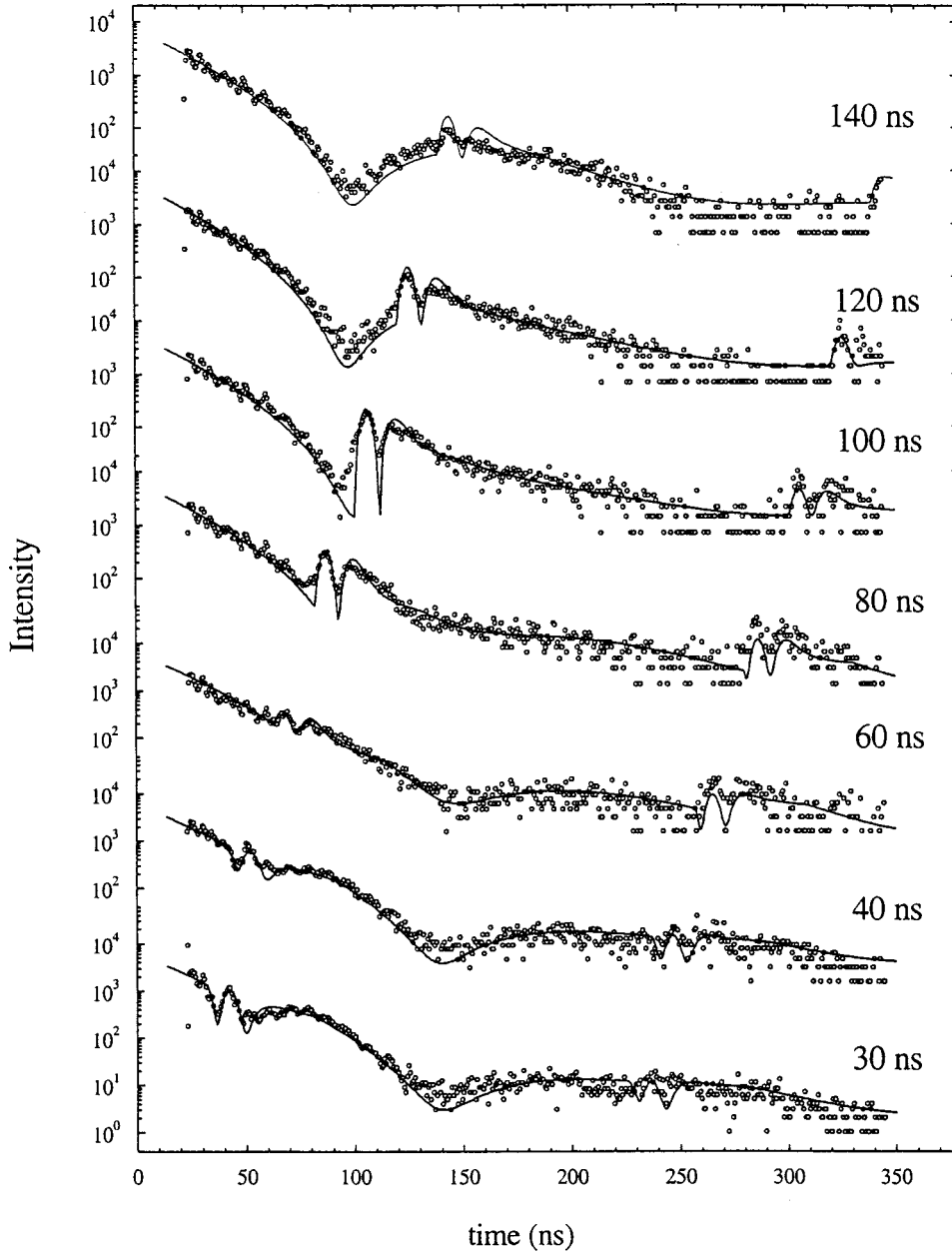where $\Theta(t-t_i)$ is the step function, being equal to zero for

FIG. 8. NFSSR of two separated SS targets recorded within a large observation window where the process of decoupling was demonstrated for the rising as well as for the falling edge of the Doppler motion profile of Fig. 5(c). The indicated values for t_d mark the start of the rising edge. The SR pulse occurred at $t = 0$ ns. QB structures are observed for both edges of the motion, proving that the coherence of the radiation fields emitted in the forward direction is preserved even when multiple velocity changes occur. Other details as in Fig. 6.

$t < t_i$ and equal to 1 for $t \geq t_i$, and t_1 is the time where the motion starts. The time intervals $(t_2 - t_1) = (t_4 - t_3)$ and $(t_3 - t_2)$ were chosen to have lengths of ~100 and ~200 ns, respectively [see Fig. 5(a)]. For the time constants we obtained $\tau_1 = \tau_3 = 14$ ns and $\tau_2 = \tau_4 = 28$ ns, and v_{max} corresponds to 21Γ with an applied voltage amplitude of 14 V. The change in phase $\varphi(t)$ between the wave fields emitted by the targets due to their relative motion caused by the piezoelectric drive is given by

$$\varphi(t) = \frac{2\pi}{\lambda_0} \int_0^t v(t')dt',\qquad (2)$$

where $\lambda_0 = 0.086$ nm is the wavelength of the 14.4 keV ra-

diation. $\varphi(t)$ is shown in the middle curve of Fig. 5(a). The maximal displacement caused by the trapezoidal motion at 14 V is 0.235 nm.

The deviations from the ideal stepwise velocity profile are clearly seen in the bottom panel of Fig. 5(a). Such deviations are expected because of the capacitorlike properties of the piezoelectric drive operated without feedback. They have been taken into account in the fitting procedure. In fact, assuming exponential-type segments, the velocity profile was independently derived by fitting the time dependences of the nuclear forward-scattering intensity directly by applying the theory for NFSSR (see Secs. III B 1 and III B 2 below). Within statistical accuracy, the agreement with Eq. (1) is very good. For this reason, to derive the velocity profiles for the other two kinds of trapezoidal motion we applied solely the NFSSR theory and not the QBA, a beam-time consuming but otherwise very fine experimental technique.
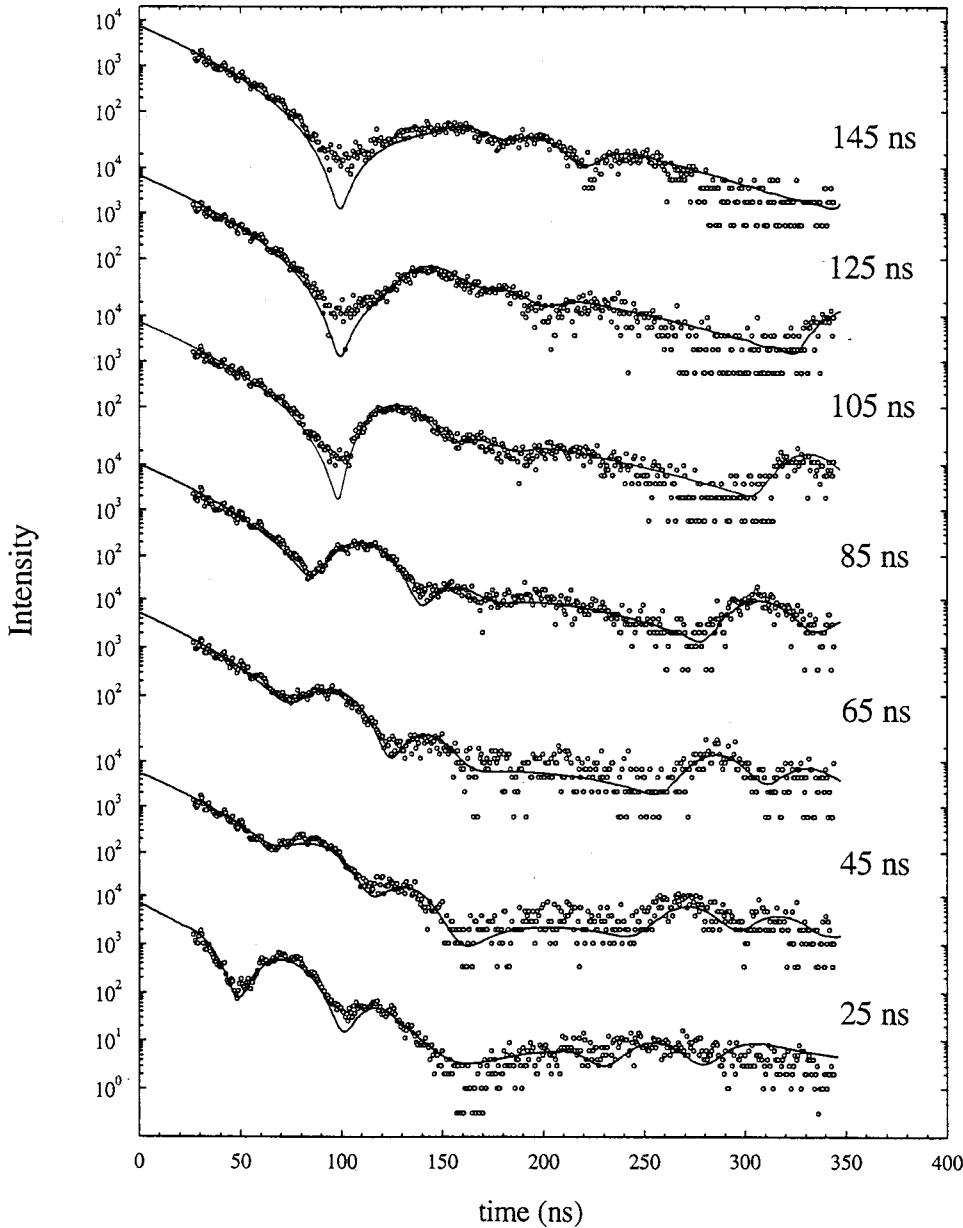
FIG. 9. Decoupling experiments for various values of t_d performed with the velocity profile of Fig. 5(b). Applying a voltage signal of 14 V a maximal Doppler shift of $\sim 21\Gamma$ was obtained, resulting in QB periods that are correspondingly longer than those in Figs. 6–8. The transition from QB dips to QB spikes via a region of reduced QB contrast for t_d between 45 and 65 ns is clearly visible.

The results for the motion profiles (b) and (c) described in Sec. II C are also depicted in Fig. 5. For profile (b) [see Fig. 5(b)] with $\Delta t_r = \Delta t_f = \Delta t_u \approx 100$ ns, the same time constants $\tau_1 = \tau_3 = 14$ ns and $\tau_2 = \tau_4 = 28$ ns as well as v_{max} corresponding to about 21Γ were obtained as for profile (a); however, $(t_3 - t_2)$ is now only 100 ns long.

The results for profile (c) [see Fig. 5(c)] are quite different: $\tau_1 = \tau_3 = 4$ ns and $\tau_2 = \tau_4 = 9$ ns. The maximum and minimum values of the velocity corresponding to $\pm 77\Gamma$ were reached after $(t_2 - t_1) = (t_4 - t_3) \approx 15$ ns. The time interval $(t_3 - t_2)$ is now ~ 185 ns long. In addition, it was assumed that 50 ns after the start of the motion the velocity has reached zero again.

B. Radiative coupling of nuclear oscillators

The central issue of this paper is the investigation of the radiative coupling field $\mathcal{R}$. This coupling field was investi-

gated for two different cases: (1) the process of decoupling of the targets, i.e., the Doppler motion of target A was started some time interval after the SR pulse; (2) the process of coupling of the targets, i.e., the Doppler motion of target A was already started before the SR pulse and then stopped after some time interval to allow the radiative coupling field to develop. For the two cases, target B was kept at rest. In the following sections the results and their theoretical description and interpretation are presented for the two types of experiment just mentioned.

1. Decoupling of the targets

a. Experimental results. Figure 6 shows the time dependences of the NFSSR intensity recorded at BW4 of the HASYLAB for various amplitudes of the voltage signal applied to the piezoelectric drive and two different decoupling times
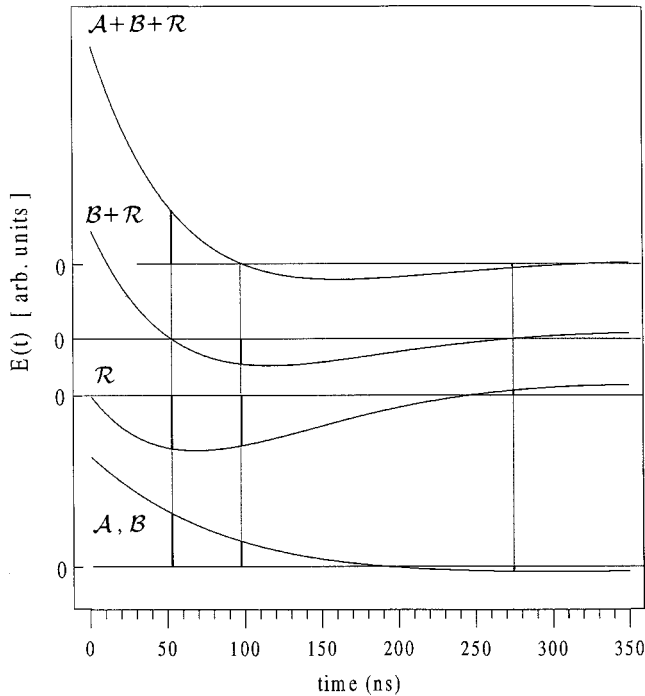
FIG. 10. Envelopes of various radiation fields according to Eq. (3) for the two-target system with both targets kept stationary $[\varphi(t)=0]$. $\mathcal{A}$ and $\mathcal{B}$ denote the responses of the targets A and B, respectively, if each target were present alone. $\mathcal{R}$ represents the radiative coupling term, i.e., the influence of the radiation field emitted by the upstream target A on the oscillators of the downstream target B. $\mathcal{B}+\mathcal{R}$ is the full response of the target B. The envelope of the radiation field recorded behind both targets together is given by $\mathcal{A}+\mathcal{B}+\mathcal{R}$. Each target is 1.2 μm thick corresponding to a Mössbauer thickness of $T\approx9.3$. For both targets natural linewidth was assumed.

t_d between the SR pulse and the onset of decoupling due to the start of the piezodrive motion. In these experiments motion profile (c) [see Fig. 5(c)] was used, which allows short rise times and large Doppler energy shifts in the range between 0 and 77Γ (see Secs. II C and III A). The left and right panels of Fig. 6 exhibit results for $t_d\approx25$ and 95 ns, respectively. In each case the SR pulse occurs at $t=0$ ns. Because of parasitic bunches and due to dead-time effects in the counter and in the gating electronics only data points for $t\geq30$ ns were taken into account in the data evaluation. The bottom panels show the results with the piezoelectric drive switched off (0 V) all the time. Here a dynamical beat (DB) pattern with a DB minimum at $t\approx100$ ns is observed, which originates from the combined target $(A+B)$ of a total thickness of 2.4 μm.

With $t_d\approx25$ ns (Fig. 6, left) and increasing Doppler shift (voltage), at first (1.75 V) the NFSSR intensity decreases more rapidly after $t=t_d$ as compared to the unperturbed (0 V) time dependence. At 3.5 V a slow quantum beat develops. The period of the QB decreases with increasing Doppler shift. At 10.6 and 14 V two periods of the QB can be recognized. Thus at high amplitudes the onset of decoupling at

$t_d\approx25$ ns can be noticed as a rapid *drop* of the NFSSR intensity toward the first QB minimum. We call this feature a *QB dip*.

With $t_d\approx95$ ns (Fig. 6, right), the motion of target A starts just slightly before the DB minimum (at $t\approx100$ ns) of the unperturbed time dependence. Up to $t=t_d$ all time dependences are the same and show the expected decrease of the intensity toward the DB minimum. After decoupling, QB patterns develop. Below ~7 V only one QB maximum can be noticed, whereas at 10.6 and 14 V two maxima are observed. In contrast to the situation with $t_d\approx25$ ns, the onset of decoupling at $t_d\approx95$ ns is found to cause a rapid *rise* of the NFSSR intensity toward the first QB maximum, a feature that we name the *QB spike*.

The transition from QB dip to QB spike patterns is demonstrated in Fig. 7 where time dependences are depicted for maximal signal amplitude (14 V) and t_d varying between 15 and 115 ns. At low values for t_d pronounced QB dips are seen. For t_d between 25 and 35 ns the contrast of the QB dips is markedly reduced. For t_d between 75 and 115 ns QB spikes with good contrast develop.

All these features were confirmed in an experiment at the ESRF storage ring where the large intensity of the SR beam allowed an observation window of 350 ns in the single-bunch mode. Again velocity profile (c) was used. Relevant time dependences are shown in Fig. 8. The two bottom curves show QB dips. For $t_d\approx60$ ns the QB contrast is lowest. For large values of t_d, QB spikes appear with a maximal contrast for $t_d\approx100$ ns. The contrast of the QB spikes at $t_d\approx140$ ns is again reduced but the QB is still visible. The long observation window made it possible to record also the onset of decoupling with the falling edge of the Doppler motion profile which occurs 200 ns after the begin of the rising edge. When the falling edge starts at $t\approx230$ ns (bottom curve) QB dips are observed with low contrast. If the falling edge begins later than $t\approx270$ ns, QB spikes with pronounced contrast develop. Between the regions of the rising and the falling edges of the trapezoidal motion there is a time interval of ~130 ns where the Doppler velocity is rather small [see Fig. 5(c)]. During this time interval radiative coupling between the targets may be restored and DB patterns may develop (see, e.g., the three lowest patterns in Fig. 8 with DB minima between 140 and 150 ns). Because of the preceding perturbation of the nuclear exciton, the DB minima are strongly shifted to later times compared to the case with the perturbation occurring very late (see top curve of Fig. 8). This restoration of coupling and its important role at later times of the NFSSR evolution will be discussed in Sec. III B 2 below.

Decoupling experiments were also performed with the two other velocity profiles, which are characterized by considerably longer times for the rising and falling edges of the trapezoidal motion and by velocity profiles [see Figs. 5(a) and 5(b)] that resemble a stepwise change more closely. As an example, Fig. 9 shows the relevant time dependences recorded at ESRF (Grenoble) with velocity profile (b). At $U=14$ V, a maximal Doppler shift of $\sim21\Gamma$ was obtained, resulting in QB periods that are correspondingly longer than those in Figs. 6–8. In Fig. 9 the main features are well dis-
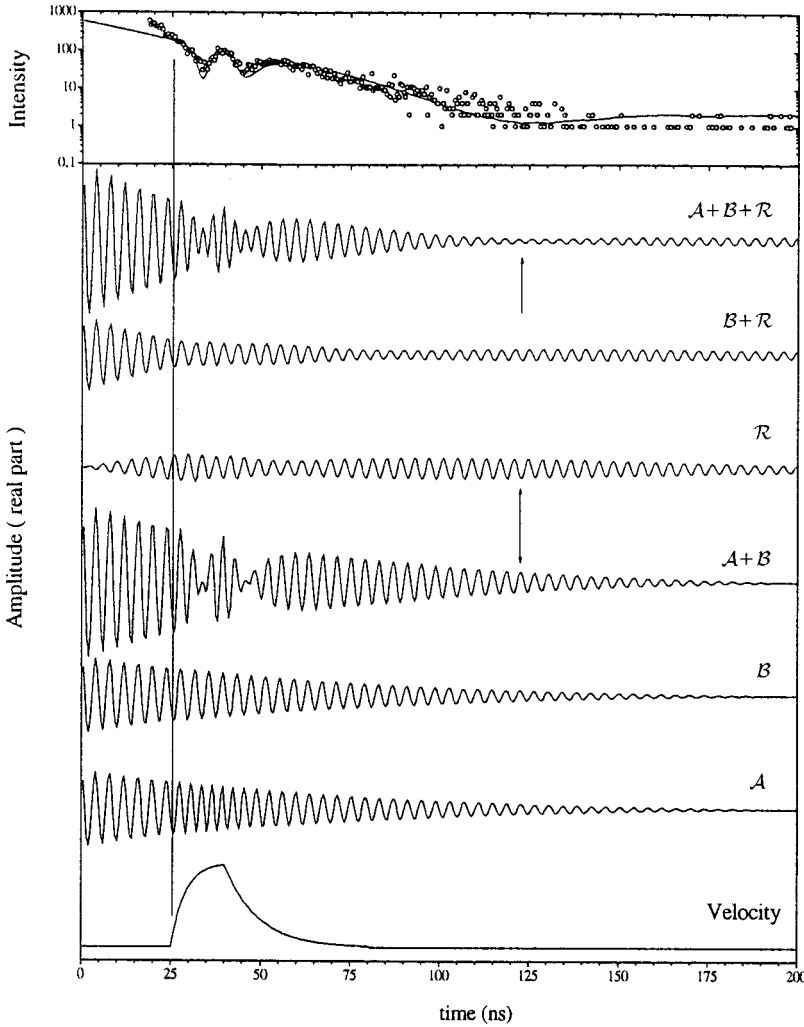
FIG. 11. Theoretical analysis according to Eq. (3) of the measured NFSSR intensity for $t_d \approx 25$ ns shown in Fig. 7. The bottom curve depicts the velocity profile (compare Fig. 5). $\mathcal{A}$ and $\mathcal{B}$ denote the real parts of the wave-field amplitudes of the individual targets, if each target were present alone. The high-frequency oscillations with an arbitrarily chosen period of ~4 ns symbolically represent the frequency of the Mössbauer radiation. This frequency changes for $\mathcal{A}$ when the upstream target A is moved by the piezoelectric drive (Doppler shift) leading to the QBs in the superposition of both fields $\mathcal{A}+\mathcal{B}$. The coupling wave field is given by $\mathcal{R}$, the full response of the downstream target B by $\mathcal{B}+\mathcal{R}$. The real part of the total field amplitude reemitted by the two-target system after the SR excitation is given by $\mathcal{A}+\mathcal{B}+\mathcal{R}$. Its intensity (full line) is compared to the experimentally determined NFSSR (dots) in the top panel. Vertical lines are intended to identify phase relations between the various wave fields. Both targets were assumed to have the same Mössbauer thickness $T=9.3$ and natural linewidth. Further details are given in the text.

played, in particular the transition from QB dips to QB spikes, including a range of reduced QB contrast for t_d between 45 and 65 ns, as well as the QB spikes for times t between ~220 and ~350 ns during the falling edge of the trapezoidal motion. Between rising and falling edges there exists a time interval of ~50 ns [see Fig. 5(b)] where the Doppler velocity is rather small and radiative coupling may be restored (see Sec. III B 2 below).

The observation of QB patterns clearly demonstrates that the radiation fields emitted from both targets are still coherent when one target is Doppler shifted by the piezoelectric drive. The time dependences in Figs. 8 and 9 show QB structures during both the rising and falling edges of the trapezoidal motion. Thus the coherence of the radiation fields emitted in the forward direction and hence a phase memory of nuclear excitations in the separated targets are preserved even in situations where multiple velocity changes occur.

b. Theoretical description and interpretation. The experimental results presented above can be understood within NF-SSR theory on the basis of the equations describing the radiation fields emitted in the forward direction by both targets. The wave field present behind both targets A and B, the intensity of which is recorded in the detector, is given by [3,5,28]

$$E(t)_{A+B} \propto \left\{ \delta(t) - (1/2\tau_0)e^{i\omega t - (q_B/2\tau_0)t} \right.$$

$$\times \left[T_A \sigma(T_A t/\tau_0)e^{i\varphi(t) - [(q_A - q_B)/2\tau_0]t} \right.$$

$$+ T_B \sigma(T_B t/\tau_0) - (1/2\tau_0)T_A T_B$$

$$\times \int_0^t dt' \, e^{i\varphi(t') - [(q_A - q_B)/2\tau_0]t'}$$

$$\left. \left. \times \sigma(T_B(t-t')/\tau_0)\sigma(T_A t'/\tau_0) \right] \right\}, \quad (3)$$

where ω is the resonance frequency of the stationary target B, $T_{A,B}$ are the effective thicknesses of the targets A,B, respectively, and τ_0 is the lifetime of the nuclear level (for ^{57}Fe, $\tau_0 \approx 141$ ns). Inhomogeneous broadening of Lorentzian type of the Mössbauer transitions can be taken into account by q_A and q_B [3]. In our samples this broadening is negligibly small. Therefore we put $q_A = q_B = 1$; also $T_A = T_B = T$. Further,

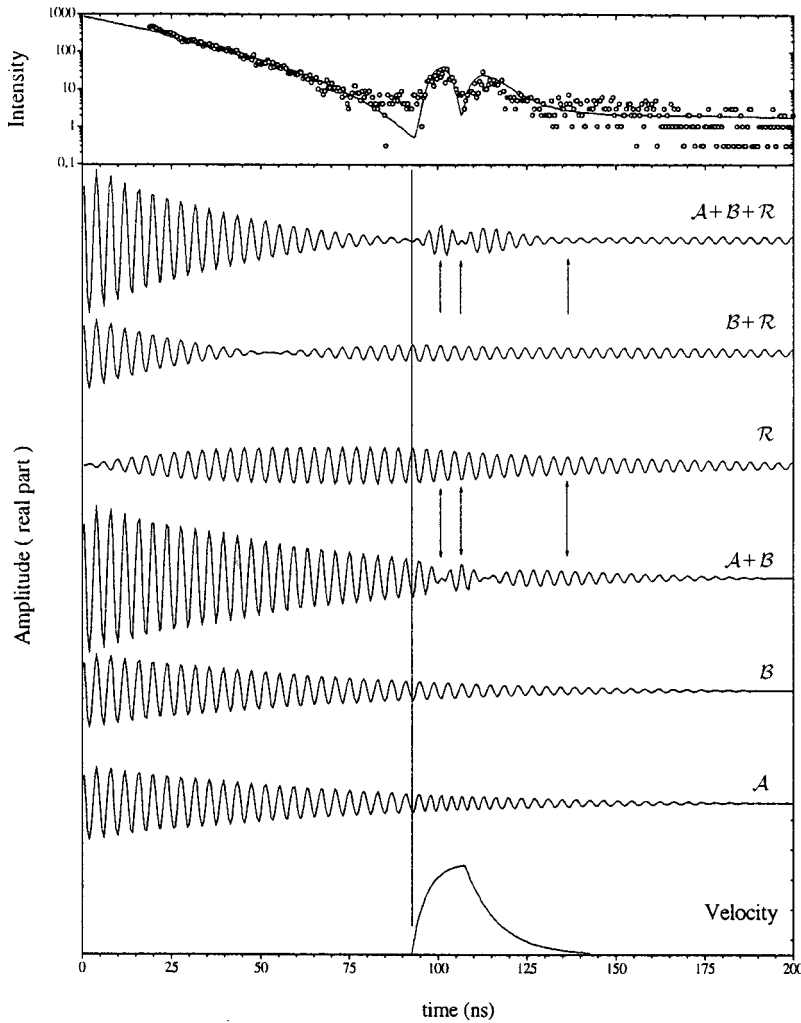$$\sigma(Tt/\tau_0) = J_1(\sqrt{Tt/\tau_0})/\sqrt{Tt/\tau_0}, \quad (4)$$

FIG. 12. Theoretical analysis of the NFSSR intensity for $t_d \approx 93$ ns shown in Fig. 7. The meaning of the symbols is the same as in Fig. 11. Note that the QB patterns at $t \approx 100$ ns of $\mathcal{A}+\mathcal{B}$ and $\mathcal{A}+\mathcal{B}+\mathcal{R}$ are in opposite phase, which is caused by the $\mathcal{R}$ wave field. For further details see the text.

with $J_1(x)$ being the Bessel function of the first kind and first order. The phase factors $e^{i\varphi(t)}$ are determined by Eq. (2) and account for the phase change between the radiation fields of the targets A and B due to the motion of target A.

Equation (3) describes four different optical paths [3,5,28,32].

(a) SR is transmitted without interaction at all. This radiation is described by the delta function $\delta(t)$.

(b) Nuclear scattering of the SR pulse occurs in target A only, represented by the first term in the square brackets. This term is called $\mathcal{A}$.

(c) Nuclear scattering of the SR pulse occurs in target B only, represented by the second term in the square brackets. This term is called $\mathcal{B}$.

(d) Nuclear scattering of the SR pulse occurs in target A *and* thereafter in target B. This multiple-scattering process is described by the integral term in the square brackets, called $\mathcal{R}$. Radiation having first excited the nuclei and dwelled in target A up to time t' excites the nuclei in the downstream target B at time t'. They are deexcited at time t. This term describes the radiative coupling, i.e., the influence of the radiation field of the upstream target on the oscillators of the downstream target. Since the integration is performed over the whole time interval $0-t$ and because the effect of radiative coupling is delayed, this term contains the full history of

excitation of the nuclei in target B by the radiation emitted from target A. Therefore $\mathcal{R}$ turns out to be important also at late times when the targets are radiatively decoupled due to the relative motion. It is interesting to note that this term has the opposite sign with respect to the first two, i.e., the wave associated with it is in antiphase to the two other waves. This phase shift of π arises from the additional resonance scattering in target B: resonance scattering by a single nucleus gives $\pi/2$, and another $\pi/2$ is due to the coherent summation of the wavelets scattered by nuclei lying in the plane wave front of the radiation (Fresnel construction).

Figure 10 shows the envelopes of the various contributions of Eq. (3) for our targets with the same thickness of $\sim 1.2~\mu$m ($T \approx 9.3$), and for $\varphi(t)=0$, i.e., in the absence of relative motion of the targets. The emitted radiation field of an individual target (bottom curve in Fig. 10) has its first DB-minimum (zero crossing of $\mathcal{A}$ and $\mathcal{B}$) at ~ 200 ns, whereas for both targets combined (resulting in a total thickness of $\sim 2.4~\mu$m) the first DB minimum occurs at ~ 100 ns (top curve of Fig. 10). The radiative-coupling term $\mathcal{R}$ [33] starts with a finite slope at $t=0$ ns [3–5], reaches its largest (negative) amplitude at ~ 70 ns, and crosses the zero line at ~ 250 ns to positive values. The latter are due to twofold scattering of the radiation emitted by target A in the downstream target B. The total radiation reemitted by target B is
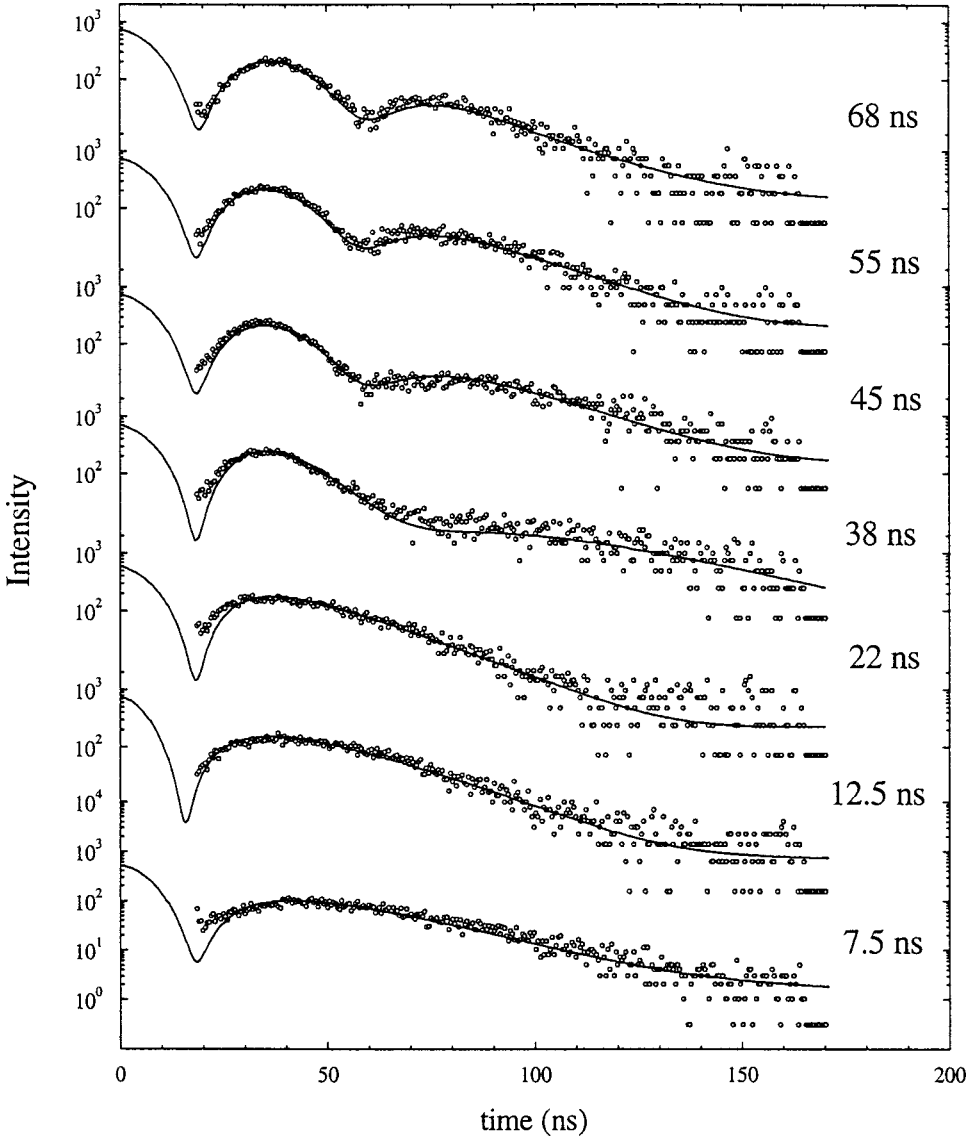
FIG. 13. NFSSR of two separated targets in coupling experiments where the velocity profile of Fig. 5(a) with a signal amplitude of 14 V was used. The times t_c given for each curve indicate the end of the rising edge [time t_2, see Fig. 5(a)] where the Doppler velocity starts to be rapidly reduced.

represented by the sum $\mathcal{B}+\mathcal{R}$ [5]. It is clearly seen that $\mathcal{R}$ is an important part of the field $\mathcal{B}+\mathcal{R}$ emitted from the target $\mathcal{B}$. Its contribution, e.g., shifts the first zero crossing of $\mathcal{B}+\mathcal{R}$ to ~50 ns and strongly increases the slope of the initial decay rate as compared to that of $\mathcal{B}$ alone.

The differences between the amplitudes of the radiation fields of the upstream and downstream targets become noticeable when a Doppler shift is applied and, as a consequence, quantum-beat patterns arise. If the Doppler motion is switched on within the time interval between $t=0$ and 50 ns after the SR pulse, the amplitudes $\mathcal{A}$ and $\mathcal{B}+\mathcal{R}$ have the same sign. Therefore, their interference starts constructively and, due to the increasing phase shift, is followed by destructive interference resulting in QB *dips* (see, e.g., the two bottom curves in Figs. 7 and 8). If the Doppler motion is switched on at $t\approx50$ ns the amplitude $\mathcal{B}+\mathcal{R}$ is close to zero and the contrast of the QB is strongly reduced (see e.g., Figs. 7 and 8, third curves from the bottom). Between $t\approx50$ and 200 ns the amplitude $\mathcal{A}$ is still positive whereas $\mathcal{B}+\mathcal{R}$ is negative. Therefore in this time interval the interference starts destructively and is followed by a QB maximum re-

sulting in QB *spikes* (see, e.g., Fig. 7, the curves for $t=75$ to 93 ns, and Fig. 8, the curves for $t=80$ to 120 ns). At $t\approx100$ ns both amplitudes have about the same absolute magnitude, leading to maximal contrast of the QB pattern. At $t\approx140$ ns the magnitude of $\mathcal{A}$ is already considerably smaller than that of $\mathcal{B}+\mathcal{R}$, and the QB contrast is again rather low (see Fig. 8, top curve).

Figure 10 being valid for two targets kept stationary depicts the basic features that characterize only the onset of decoupling at $t=t_d$. However, to interpret the entire time dependences during the time interval where the Doppler motion is activated and also for times thereafter the theoretical description using Eq. (3) with the phase factors $e^{i\varphi(t)}$ is required. While before the motion started these phase factors were equal to unity, they now play a decisive role, since they affect both the wave field reemitted by target A and the coupling term. As examples, this is demonstrated for two cases where $t_d=25$ and 93 ns.

For $t_d=25$ ns, the various terms of Eq. (3) are depicted in Fig. 11, which analyzes the corresponding time dependence shown in Fig. 7. In Fig. 11, the description in terms of wave
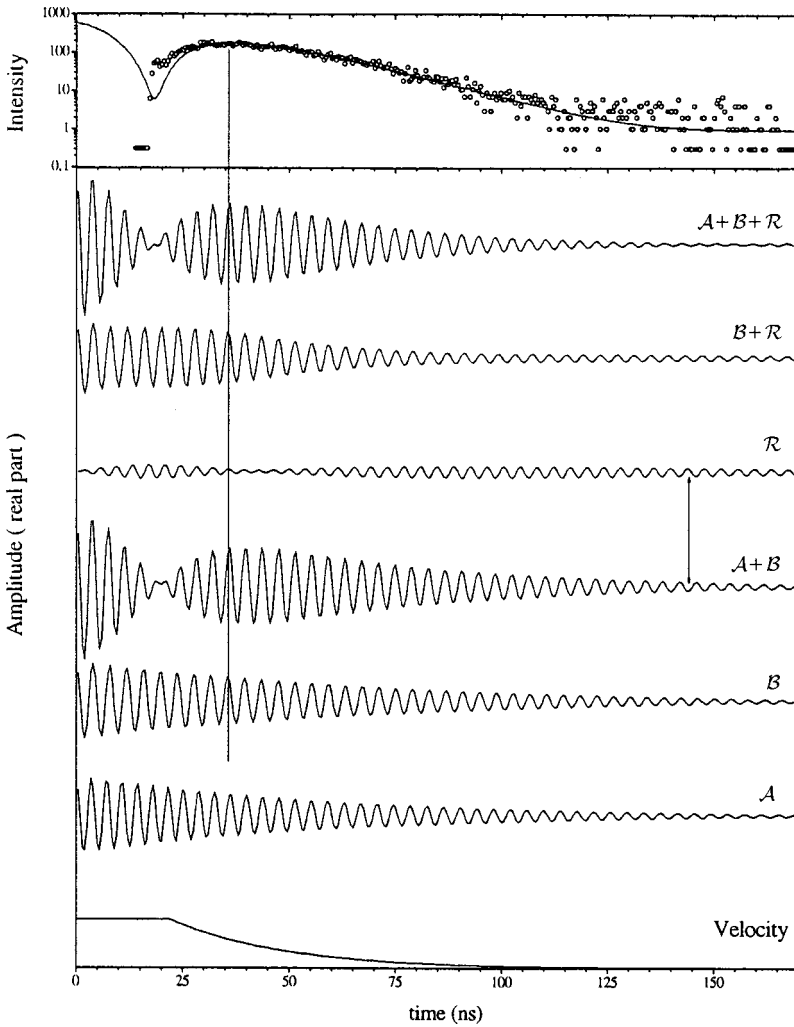
FIG. 14. Theoretical analysis of the NFSSR intensity for $t_c = 22$ ns shown at the top and in Fig. 13. The total amplitude $\mathcal{A} + \mathcal{B} + \mathcal{R}$ is essentially determined by the $\mathcal{A} + \mathcal{B}$ field except for very late times where the $\mathcal{R}$ field is the bigger contribution. Further details as in Fig. 11.

packets is applied where both wave amplitude and phase are important. For the electric wave fields always the real part is displayed in the figure. The shape of the wave packet representing the total field $\mathcal{A} + \mathcal{B} + \mathcal{R}$ is obtained as the result of a theoretical analysis according to Eq. (3) for the measured time dependence of the NFSSR intensity (see top panel in Fig. 11). The high-frequency oscillations with a period of $\sim$4 ns shown in Fig. 11 symbolically represent the actual frequency of the Mössbauer radiation of $\omega_0 \approx 10^{19} \, \mathrm{s}^{-1}$ for ^{57}Fe. The lowest wave-field curve characterizes the wave field emitted by the upstream target A. Within the time interval between 25 and 70 ns, the frequency of $\mathcal{A}$ is modulated according to the velocity profile of the piezoelectric drive shown at the bottom of Fig. 11. The frequency of $\mathcal{B}$ remains unaffected. The interference of these two wave fields, $\mathcal{A} + \mathcal{B}$, displays the amplitude modulation due to the different frequencies of the waves $\mathcal{A}$ and $\mathcal{B}$. The relative maximum of $\mathcal{A} + \mathcal{B}$ at $t \approx 65$ ns shows that $\mathcal{A}$ and $\mathcal{B}$ are nearly in phase again at the end of the motion of target A.

Up to $t \approx t_d = 25$ ns there is no Doppler motion, both targets are fully coupled, and the $\mathcal{R}$ field is built up. During the interval where the Doppler motion is on, radiative coupling between the targets is nearly excluded. Nevertheless, due to the preceding coupling an appreciable $\mathcal{R}$ field is emitted by target B. However, the field amplitude is now gradually de-

creasing. When the Doppler velocity is again low (at $t \approx 60$ ns), i.e., comparable to the linewidth in the SS, both targets are again coupled and the $\mathcal{R}$ field reaches another (although broad) maximum around $t \approx 125$ ns. Up to $t \approx t_d$, $\mathcal{R}$ is exactly in antiphase to $\mathcal{B}$. Thereafter, due to the phase factor $e^{i\varphi(t')}$ in Eq. (3), the phase relation between $\mathcal{B}$ and $\mathcal{R}$ is slightly different from π. As a consequence, the field amplitude $\mathcal{B} + \mathcal{R}$ does not reach zero, in contrast to the case of full coupling.

The total field amplitude $\mathcal{A} + \mathcal{B} + \mathcal{R}$ can be discussed in terms of two different superpositions: $\mathcal{A} + (\mathcal{B} + \mathcal{R})$ or $(\mathcal{A} + \mathcal{B}) + \mathcal{R}$. These two presentations allow us to get a more complete insight into the interference of the constituent fields. The first presentation, for example, was used in Fig. 10 to explain the onset of QB dips and QB spikes. The second description can reveal different aspects of the QB modulation in $\mathcal{A} + \mathcal{B} + \mathcal{R}$. For instance, the two QB minima at $\sim$35 and 45 ns occur nearly at the same time as those of $\mathcal{A} + \mathcal{B}$, although with slightly reduced contrast. This similarity is present because up to $t \approx 100$ ns the $\mathcal{R}$ amplitude is considerably smaller than the $\mathcal{A} + \mathcal{B}$ term. For $t \approx 125$ ns, however, both fields have comparable amplitudes and being opposite in phase they yield another minimum of $\mathcal{A} + \mathcal{B} + \mathcal{R}$, whereas there is no minimum in $\mathcal{A} + \mathcal{B}$. For $t > 125$ ns, the $\mathcal{R}$
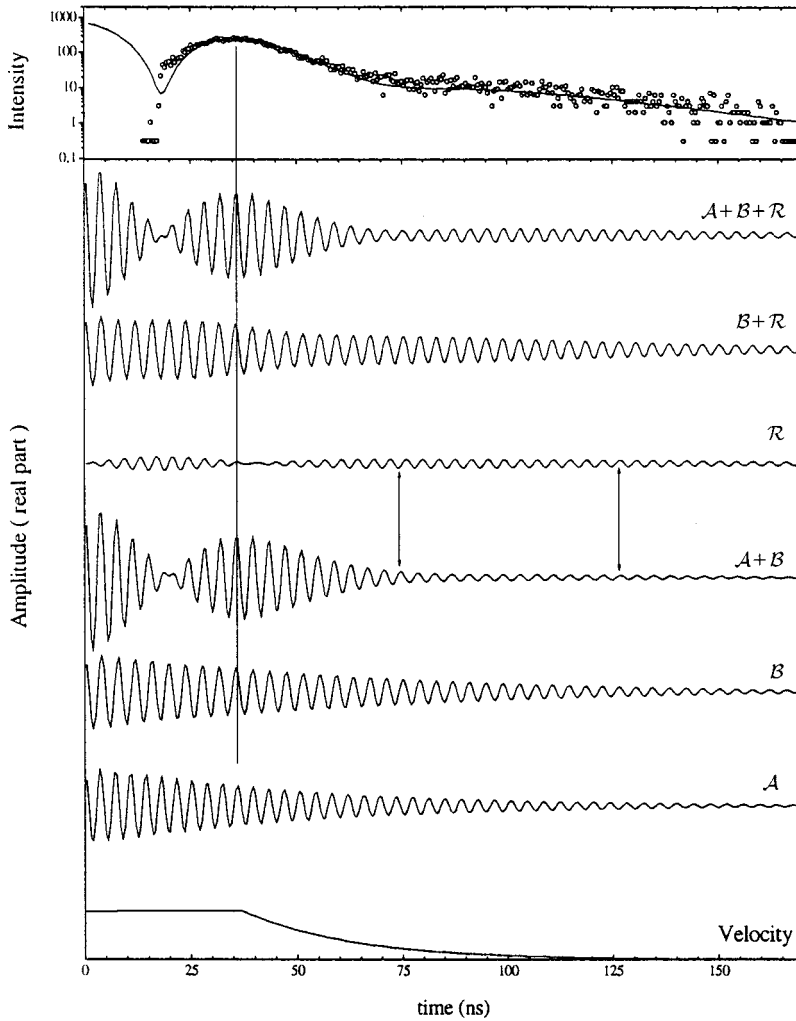
FIG. 15. Theoretical analysis of the NFSSR intensity for $t_c = 38$ ns shown at the top and in Fig. 13. At this value of t_c, the $\mathcal{A} + \mathcal{B}$ field nearly vanishes for $t \gtrsim 75$ ns and the $\mathcal{R}$ field remains the dominant contribution to the NFSSR intensity. Further details as in Fig. 11.

amplitude gives the dominant contribution and is responsible for the late increase of $\mathcal{A} + \mathcal{B} + \mathcal{R}$. All these features of $\mathcal{A} + \mathcal{B} + \mathcal{R}$ are observed in the measured time evolution of the intensity as demonstrated by the data points in the top panel of Fig. 11. In particular, the minimum and the late increase of $\mathcal{A} + \mathcal{B} + \mathcal{R}$ can also be clearly recognized in the bottom curve of Fig. 8, which shows the intensity evolution measured at the ESRF for a similar switching time as for Fig. 11, but with higher count rate.

We have performed a similar analysis for $t_d = 93$ ns, i.e., when the motion of the piezoelectric drive starts close to the time where the first DB minimum is observed (see the bottom curve of Fig. 6). This case corresponds to the experimental data for $t_d = 93$ ns in Fig. 7. Qualitatively, our analysis also applies to the experimental data obtained with $t_d = 80$ and 100 ns for a larger observation window at the ESRF (see Fig. 8, third and fourth curves from the top). The results of our analysis are shown in Fig. 12. Because the radiative coupling between the targets lasts for a long time (right from the beginning at $t = 0$) the $\mathcal{R}$ field can fully develop. At the start of the Doppler motion the fields $\mathcal{A}$ and $\mathcal{B} + \mathcal{R}$ have about the same amplitudes but opposite phases. Therefore, as discussed in the context of Fig. 10, their interference in $\mathcal{A} + \mathcal{B} + \mathcal{R}$ starts destructively with high contrast and is characterized by a QB spike when the fields come to the same phase.

We again make an analysis of the QB pattern in the total field in terms of the alternative superposition $(\mathcal{A} + \mathcal{B}) + \mathcal{R}$. In contrast to the previous case ($t_d = 25$ ns, compare Fig. 11), now the decoupling occurs at a rather late time. Therefore the term $\mathcal{R}$ is important in the whole observation window displayed in Fig. 12. Essentially for all times $\mathcal{R}$ interferes destructively with $\mathcal{A} + \mathcal{B}$. For the present case of decoupling close to a DB minimum, $\mathcal{R}$ has about the same absolute amplitude as $\mathcal{A} + \mathcal{B}$, as seen from Fig. 12 (compare also Fig. 10 for $t = 100$ ns). Hence, when $\mathcal{A} + \mathcal{B}$ displays a maximum at $t \approx 110$ ns, $\mathcal{A} + \mathcal{B} + \mathcal{R}$ has about vanishing amplitude, while at neighboring times when $\mathcal{A} + \mathcal{B}$ has nodes of zero amplitude, $\mathcal{A} + \mathcal{B} + \mathcal{R}$ reflects the relatively large amplitude of the term $\mathcal{R}$ alone. As a consequence, around $t = 100$ ns the interference pattern of the total field $\mathcal{A} + \mathcal{B} + \mathcal{R}$ is almost opposite in phase to that of $\mathcal{A} + \mathcal{B}$. Moreover, one can say that the maxima of the QB pattern of the measured intensity evolution reveal the contribution of the field $\mathcal{R}$ alone. Close to the end of the Doppler motion (at $t \approx 140$ ns) the $\mathcal{R}$ term is comparable to the $\mathcal{A} + \mathcal{B}$ contribution, yielding a weak DB minimum at $t \approx 140$ ns, and thereafter it dominates the $\mathcal{A} + \mathcal{B}$ contribution, leading to a slight rise of the $\mathcal{A} + \mathcal{B} + \mathcal{R}$ amplitude. Thus, contrary to the situation for $t_d = 25$ ns, in the present case where decoupling occurs at a time close to a DB minimum, the observed modulation pattern (see top

curve of Fig. 12) is not mainly determined by $\mathcal{A}+\mathcal{B}$ but by an intricate interference of the $\mathcal{A}$, $\mathcal{B}$, and $\mathcal{R}$ wave fields.

2. Coupling of the targets

In Sec. III B 1 we considered experiments where the SR pulse occurred at a time when both targets where at rest. Some time interval later the upstream target A was Doppler shifted relative to the downstream target B and the process of decoupling was investigated. We now turn to experiments where the excitation by the SR pulse takes place at a time when target A is being Doppler shifted relative to target B and some time interval later the motion of the target A is abruptly stopped. In this way we studied the onset and further development of radiative coupling between the targets.

a. Experimental results. In analogy to the decoupling experiments we first used the velocity profile (c) allowing a maximal Doppler shift of $\sim 77\Gamma$ for such coupling experiments. However, we found it difficult to stop the motion of the target A abruptly from high Doppler velocities [see, e.g., Fig. 5(c)]. Therefore another set of time dependences of the NFSSR intensity was recorded using the more "gentle" velocity profile (a) of Fig. 5(a) (see Secs. II C and III A). Figure 13 exhibits the results. In all cases shown the motion of the target A already begins before the SR pulse arrives at $t=0$. Thus the resulting QB always starts with a maximum at $t=0$. The times t_c given in Fig. 13 indicate the end of the rising edge at time t_2 of the trapezoidal displacement [see Fig. 5(a)] where the Doppler velocity starts to be rapidly reduced. With decreasing t_c, the shapes of the NFSSR patterns change strongly. For t_c between 68 and 45 ns two QB minima are observed. At $t_c=38$ ns the second minimum is shifted to later times by about 10 ns, and for still lower values of t_c the NFSSR intensity drops more gradually and this minimum can no longer be discerned. According to Fig. 5(a) the actual onset of radiative coupling occurs about 25 ns after t_c. Two characteristic cases of Fig. 13 will be analyzed in the following section.

b. Theoretical description and interpretation. Similar to the procedure described in Sec. III B 1 for the case of decoupling, the data were again analyzed according to the four different optical paths [see Eq. (3)] contributing to the total wave field behind the targets, which gives rise to the NFSSR intensity recorded in the detector.

We discuss two cases of Fig. 13 in more detail. For a proper analysis of the data, we had to assume that the piezoelectric motion exhibited a spread in maximum velocity of $\sim 10\%$. Figure 14 shows the analysis for the NFSSR pattern obtained at $t_c=22$ ns (see Fig. 13 and top panel of Fig. 14). As before, the constituents of the total wave packet according to Eq. (3) are displayed in the lower panels. Due to the Doppler motion of the target A, the $\mathcal{A}+\mathcal{B}$ field exhibits a QB pattern with the first minimum at $t\approx 20$ ns and the following maximum at $t\approx 40$ ns. Thereafter, the $\mathcal{A}$ and $\mathcal{B}$ fields interfere constructively and the $\mathcal{A}+\mathcal{B}$ field diminishes rather slowly. The $\mathcal{R}$ amplitude is small in the whole observation window and in antiphase to the $\mathcal{A}+\mathcal{B}$ field for $t\gtrsim 50$ ns. Thus the total amplitude $\mathcal{A}+\mathcal{B}+\mathcal{R}$ is essentially determined by $\mathcal{A}+\mathcal{B}$ except for late times where destructive interference

between $\mathcal{A}+\mathcal{B}$ and $\mathcal{R}$ leads to a minimum of $\mathcal{A}+\mathcal{B}+\mathcal{R}$ at $t\approx 150$ ns. Thereafter $\mathcal{R}$ remains the biggest contribution. Figure 15 shows the analysis for the NFSSR pattern obtained at $t_c=38$ ns (Fig. 13, fourth curve from the bottom, top panel in Fig. 15). With $t_c=38$ ns, the decreasing Doppler motion causes the $\mathcal{A}+\mathcal{B}$ field to nearly vanish for $t\gtrsim 75$ ns. The amplitude $\mathcal{R}$ is rather small during the whole observation window, because at early times the energy of target A is Doppler shifted and at later times ($t\gtrsim 75$ ns), where the Doppler motion is rather slow, the $\mathcal{A}$ field already exhibits relatively small amplitude. That is why the QB in $\mathcal{A}+\mathcal{B}$ is closely reproduced in the total field $\mathcal{A}+\mathcal{B}+\mathcal{R}$. However, since the $\mathcal{A}+\mathcal{B}$ field is nearly nil, the $\mathcal{R}$ field is the dominant contribution for $t\gtrsim 75$ ns. The $\mathcal{R}$ field being in antiphase to the $\mathcal{A}+\mathcal{B}$ field around $t=75$ ns and coming into phase about 25 ns later causes the total scattering amplitude $\mathcal{A}+\mathcal{B}+\mathcal{R}$ to exhibit a minimum at $t\approx 75$ ns and a broad maximum at $t\approx 100$ ns. This is one of the surprising cases where mainly the $\mathcal{R}$ field determines the pattern of the NFSSR intensity after the motion of target A has come close to a stop. It was achieved by stopping the motion at a time when the $\mathcal{A}$ and $\mathcal{B}$ fields nearly cancel.

It is rather difficult to stop the motion of a mechanical system on a nanosecond scale without using feedback. As can be seen in Fig. 15, the velocity profile has a rather long tail after $t=t_c=38$ ns, although in this experiment the profile of type (a) with a relatively low $v_{max}\approx 21\Gamma$ was used [see Fig. 5(a) and Secs. II C and III A]. It is interesting to theoretically simulate an experiment where this velocity tail is assumed to be much shorter, i.e., where the profile comes close to an ideal step function. The results of the simulations are shown in Fig. 16. The motion stops where the $\mathcal{A}$ and $\mathcal{B}$ fields are in antiphase (at $t\approx 50$ ns). For $t\lesssim 50$ ns, the QB is clearly seen in the interference pattern $\mathcal{A}+\mathcal{B}$; thereafter the $\mathcal{A}$ and $\mathcal{B}$ fields interfere destructively and the $\mathcal{A}+\mathcal{B}$ wave field is zero for all times. The $\mathcal{R}$ field is small for $t\lesssim 50$ ns, because target A is Doppler shifted. After the motion stops, $\mathcal{R}$—as expected—increases to a maximum at $t\approx 100$ ns and thereafter it decreases again. Since the $\mathcal{A}+\mathcal{B}$ field is zero, the total field $\mathcal{A}+\mathcal{B}+\mathcal{R}$ is solely determined by the $\mathcal{R}$ field for $t>50$ ns. Thus, if an experiment were performed with such a velocity profile, the NFSSR intensity recorded for $t>50$ ns would allow one to determine the $\mathcal{R}$ term alone. Unfortunately, our piezoelectric drive was not able to stop so abruptly. Figure 13 ($t_c=38$ ns) and Fig. 15 depict the results that came closest to the aim of studying the onset and the further development of the $\mathcal{R}$ field itself.

IV. CONCLUSIONS

We have investigated the radiative coupling between two spatially separated ensembles of nuclear oscillators (two SS foils) mounted one behind the other in a SR beam by moving the upstream target in a trapezoidal-type displacement profile on a nanosecond time scale. The motion was accomplished by a piezoelectric PVDF foil subject to trapezoidal voltage changes synchronized with the SR pulse. The motion of the SS foil was calibrated using the method of quantum-beat analysis and was independently derived by a fitting proce-
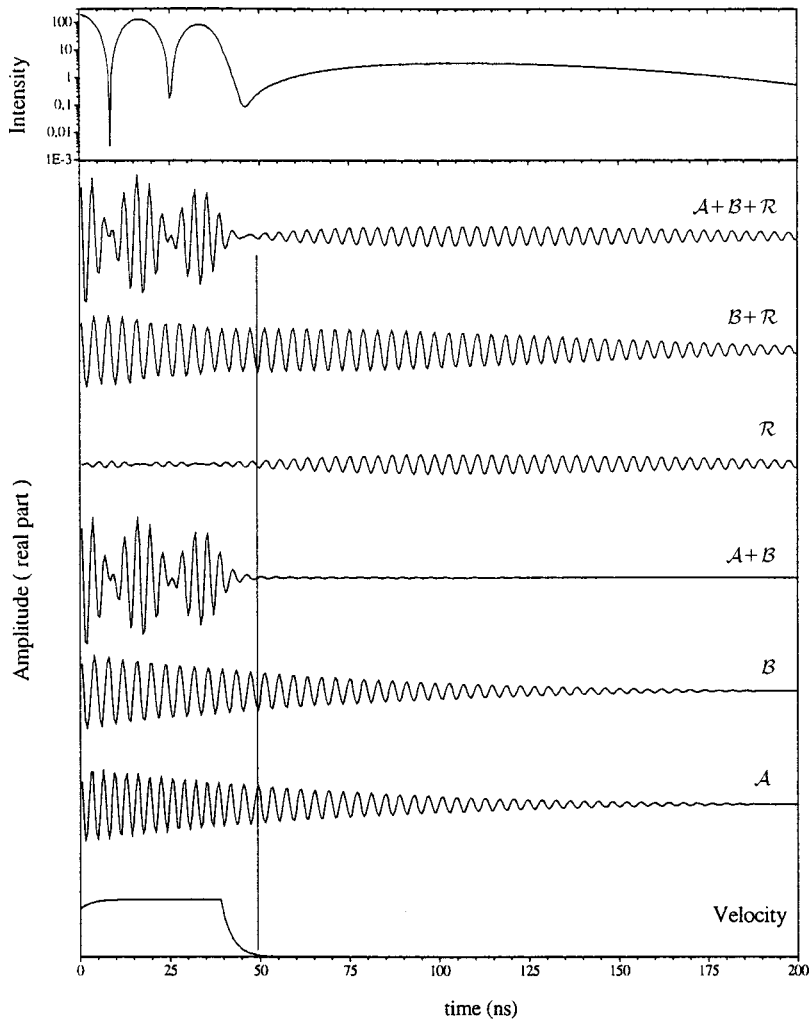
FIG. 16. Theoretical simulation of an experiment where a more advanced piezoelectric drive would allow one to stop the motion of the upstream target more abruptly. If the motion is stopped at a time ($t \approx 50$ ns) where the $\mathcal{A}$ and $\mathcal{B}$ fields are in antiphase, only the $\mathcal{R}$ field remains for all times thereafter. In such an experiment the behavior of the $\mathcal{R}$ field alone could be investigated.

dure based on NFS theory. Two different types of experiment were performed. (1) Decoupling experiments: to investigate the decoupling process, the two SS foils were kept at rest when the SR pulse occurred. Some time interval later the upstream target was Doppler shifted by the PVDF drive relative to the downstream target. (2) Coupling experiments: the SR pulse arrived at a time when the upstream foil was already in motion. Some time interval later the motion of the target was stopped. In this way the onset of coupling and its evolution were studied.

After decoupling, a pronounced QB is observed, the period of which is determined by the Doppler shift due to the motion between the targets. A remarkable feature is the transition in the appearance of the QB when the switching time was changed. When the motion was switched on early after the SR pulse, QB dips developed. With increasing switching times the QB contrast passed through a minimum and QB spikes were observed when switching at late times occurred. Our theoretical analysis on the basis of NFS theory shows that this behavior is caused by radiative coupling between the two foils, which is still weak at early switching times but plays a decisive role when the motion is switched on at late times. It was shown that the maxima in the observed spikes of NFS at late times are mainly due to the $\mathcal{R}$ field.

The onset of radiative coupling can be investigated best if the motion of the upstream target is abruptly stopped at a moment when the QB pattern is close to a minimum. Then the NFSSR intensity observed thereafter is determined by radiative coupling. Although it was not possible to bring our piezoelectric drive to a sudden stop, we were able to show the dominant importance of the radiative coupling field for a large time interval.

In all experiments performed in this investigation, the sequence of the targets does not matter since both targets were chosen to be identical. However, if, for example, the thickness of the targets or the resonance width of the oscillators in each foil were different [5], the radiation field observed behind both targets could very well depend on the target sequence. Theoretical simulations show that in these cases also radiative coupling is a prominent feature. This question will be addressed in future investigations.

[1] G. V. Smirnov, Hyperfine Interact. **97/98**, 551 (1996); in *X-Ray and Inner-Shell Processes*, edited by R. L. Johnson, H. Schmidt-Böcking, and B. F. Sonntag, AIP Conf. Proc. No. **389** (AIP, Woodbury, NY, 1997), p. 323.

[2] *Nuclear Resonant Scattering of Synchrotron Radiation*, edited by E. Gerdau and H. de Waard, Part A, Chaps. II, III.1, and IV.2 [Hyperfine Interact. **123/124** (1999)].

[3] G. V. Smirnov, Hyperfine Interact. **123/124**, 31 (1999).

[4] W. Potzel, in *Condensed Matter Studies by Nuclear Methods, Proceedings of XXXIV Zakopane School of Physics*, edited by E. A. Görlich and A. T. Pedziwiatr (Wydawnictwo Uniwersytetu Jagiellonskiego, Krakow, 1999), p. 95.

[5] W. Potzel, U. van Bürck, P. Schindelmann, G. M. Kalvius, G. V. Smirnov, E. Gerdau, Yu. V. Shvyd'ko, H. D. Rüter, and O. Leupold, Phys. Rev. A **63**, 043810 (2001).

[6] J. B. Hastings, D. P. Siddons, U. van Bürck, R. Hollatz, and U. Bergmann, Phys. Rev. Lett. **66**, 770 (1991).

[7] Yu. Kagan, A. M. Afanas'ev, and V. G. Kohn, J. Phys. C **12**, 615 (1979).

[8] J. P. Hannon and G. T. Trammell, in *Resonant Anomalous X-Ray Scattering*, edited by G. Materlik, C. J. Sparks, and K. Fischer (North-Holland, Amsterdam, 1994), p. 565.

[9] U. van Bürck, Hyperfine Interact. **123/124**, 483 (1999).

[10] U. van Bürck, W. Potzel, P. Schindelmann, Yu. V. Shvyd'ko, E. Gerdau, O. Leupold, and H. D. Rüter, Phys. Rev. A **61**, 013803 (2000).

[11] D. C. Burnham and R. Y. Chiao, Phys. Rev. **188**, 667 (1969).

[12] Yu. Kagan, Hyperfine Interact. **123/124**, 83 (1999).

[13] J. P. Hannon and G. T. Trammell, Hyperfine Interact. **123/124**, 127 (1999).

[14] Yu. V. Shvyd'ko, Phys. Rev. B **59**, 9132 (1999); Hyperfine Interact. **123/124**, 275 (1999).

[15] D. P. Siddons, J. B. Hastings, and G. Faigel, Nucl. Instrum. Methods Phys. Res. A **266**, 329 (1988).

[16] The high-resolution monochromator that was used at HASY-LAB (Hamburg) employs channel-cut Si(4 2 2) and Si(12 2 2) crystals in the nested geometry. It was designed by E. Gerdau, R. Rüffer, and H. D. Rüter based on a proposal by T. Ishikawa, Y. Yoda, K. Izumi, C. K. Suzuki, X. W. Zhang, M. Ando, and S. Kikuta, Rev. Sci. Instrum. **63**, 1015 (1992). For further details, see O. Leupold, E. Gerdau, H. D. Rüter, W. Meyer-Klaucke, A. X. Trautwein, and H. Winkler, HASYLAB Annual Report I, 1996 (unpublished), p. 73. A similar high-resolution monochromator was used at ESRF (Grenoble).

[17] A. Q. R. Baron, Nucl. Instrum. Methods Phys. Res. A **352**, 665 (1995).

[18] A. Q. R. Baron, R. Rüffer, and J. Metge, Nucl. Instrum. Methods Phys. Res. A **400**, 124 (1997).

[19] S. Kishimoto, J. Synchrotron Radiat. **5**, 275 (1998).

[20] G. von Eynatten, E. Fukada, and K. Dransfeld, Hyperfine Interact. **42**, 1095 (1988).

[21] G. von Eynatten and K. Dransfeld, Hyperfine Interact. **58**, 2555 (1990).

[22] P. Helistö, I. Tittonen, M. Lippmaa, and T. Katila, Phys. Rev. Lett. **66**, 2037 (1991).

[23] I. Tittonen, M. Lippmaa, P. Helistö, and T. Katila, Phys. Rev. B **47**, 7840 (1993).

[24] Characteristics of Kynar Piezo Film, AMP Incorporated (Elf Atochem Sensors, Inc.), P.O. Box 799, Valley Forge, PA 19482.

[25] P. Schindelmann, Ph.D. thesis, 1999, Physik-Department E15, Technische Universität München, D-85748 Garching, Germany.

[26] U. van Bürck, D. P. Siddons, J. B. Hastings, U. Bergmann, and R. Hollatz, Phys. Rev. B **46**, 6207 (1992).

[27] U. van Bürck, W. Potzel, P. Schindelmann, G. V. Smirnov, S. L. Popov, E. Gerdau, O. Leupold, Yu. V. Shvyd'ko, and H. D. Rüter, HASYLAB Annual Report I, 1996 (unpublished), p. 888.

[28] G. V. Smirnov and W. Potzel, Hyperfine Interact. **123/124**, 633 (1999).

[29] A. Ludwig and H. Jex, Physica B **254**, 1 (1998).

[30] A. Q. R. Baron, H. Franz, A. Meyer, R. Rüffer, A. I. Chumakov, E. Burkel, and W. Petry, Phys. Rev. Lett. **79**, 2823 (1997).

[31] Yu. V. Shvyd'ko, Hyperfine Interact. **125**, 173 (2000). The program was implemented in the code MOTIF by Yu. V. Shvyd'ko.

[32] G. V. Smirnov, V. G. Kohn, and W. Petry, Phys. Rev. B **63**, 144303 (2001).

[33] In Ref. [5] it was shown that for two stationary targets with nuclear oscillators exhibiting natural linewidth, the wave field $\mathcal{B}+\mathcal{R}$ can be obtained in analytical form by subtracting the wave field $\mathcal{A}$ from the field $\mathcal{A}+\mathcal{B}+\mathcal{R}$ observed behind the combined target $(A+B)$ of total Mössbauer thickness $T_{A+B} = T_A + T_B$. Similarly, the coupling field $\mathcal{R}$ can directly be derived by subtracting the wave fields $\mathcal{A}$ and $\mathcal{B}$ of the individual targets from the field $\mathcal{A}+\mathcal{B}+\mathcal{R}$. In the case of nonstationary targets or additional line broadening such a procedure cannot be applied and Eq. (3) has to be used and evaluated numerically.